OPTICS

# Twisted black phosphorus–based van der Waals stacks for fiber-integrated polarimeters

Yifeng Xiong[1]†, Yushu Wang[1]†, Runze Zhu[1]†, Haotian Xu[1], Chenhui Wu[1], Jinhui Chen[2], Yang Ma[1], Yuan Liu[1], Ye Chen[1], Kenji Watanabe[3], Takashi Taniguchi[4], Mengzhu Shi[5,6], Xianhui Chen[5,6], Yanqing Lu[1], Peng Zhan[7], Yufeng Hao[1]*, Fei Xu[1]*



**The real-time, in-line analysis of light polarization is critical in optical networks, currently suffering from complex systems with numerous bulky opto-electro-mechanical elements tandemly arranged along the optical path. Here, we design and fabricate a fiber-integrated polarimeter by vertically stacking three photodetection units based on six-layer van der Waals materials, including one bismuth selenide ($Bi_2Se_3$) layer for power calibration, two twisted black phosphorus (BP) layers for polarization detection, and three hexagonal boron nitride (hBN) layers for encapsulation. The self-power-calibrated, self-driven, and unambiguous detection of both linearly polarized (LP) and circularly polarized (CP) light is realized by the broken symmetry–induced linear photogalvanic effects (LPGEs) and circular photogalvanic effects (CPGEs) in the two BP units. Moreover, the device enables single-pixel polarimetric imaging to acquire spatial polarization information. The ultracompact device structure, free from external optical and mechanical modules, may inspire the development of miniaturized optical and optoelectronic systems.**

## INTRODUCTION

Polarization, one of the fundamental characteristics in communication, imaging, navigation, sensing, and almost all optics-related fields (*1*–*3*), is crucial in optical networks. Traditional polarimeters used in the optical network require a series of opto-electro-mechanical elements (including lenses, prisms, polarizers, wave plates, filters, photodetectors, and mechanical parts) tandemly arranged along the optical path, which is difficult to minimize and integrate for compact applications (*1*, *4*). The realization of an ultracompact polarimeter requires breakthroughs in the two main aspects: (i) the downsizing of bulky components and the compression of the optical path to nano- and micrometer scale, getting rid of any external optical and mechanical modules, and (ii) fast, unambiguously high-performance detection of multiple polarization states, including linearly polarized (LP) and circularly polarized (CP) light.

To solve the problems, several polarization-sensitive photodetectors have been investigated using natural anisotropic two-dimensional (2D) materials with low crystal symmetry, such as black phosphorus (BP), $ReS_2$, GeSe, and van der Waals (vdW) interfaces (*5*–*18*). However, these photodetectors need additional power meters to decouple the illumination power–polarization relationship. Meanwhile, such devices cannot precisely distinguish the actual polarization state of light since the polarized photocurrents exist overlap at different polarization angles. Artificial plasmonic structures have recently been investigated as additional filter layers to build polarization-sensitive photodetectors (*19*–*23*). However, these structures usually require an array of nanoantenna units to accumulate photocurrent, resulting in an increase in the device size and will cause unnecessary energy loss. In addition, the above devices are still challenging to distinguish the photocurrent generated by LP or CP light.

In this work, we demonstrate an ultracompact polarimeter by vertically stacking three photodetection units based on 2D vdW materials onto an optical fiber endface. We choose an isotropic $Bi_2Se_3$ as the calibration unit to monitor the illumination power, which is polarization insensitive to incident light and has a narrow bandgap of 0.3 eV (*24*). Two anisotropic BP units are then twistedly stacked for polarized photosensing, which have direct bandgap (0.3 eV for multilayer), high mobility, and anisotropic optoelectronic properties (*10*, *25*–*27*). The asymmetrically designed electrodes against the fiber core in BP units break the system symmetry and lead to linear photogalvanic effect (LPGE) and circular photogalvanic effect (CPGE), showing a high-contrast and self-driven photoresponse to both LP and CP light. With the power calibration unit, the different polarized photocurrents generated from the twisted BP units lead to an unambiguous detection of polarized light, without any external optical components or mechanical parts. Furthermore, by applying time-varying Hadamard patterns and measuring synchronized photocurrents, we achieve single-pixel polarimetric imaging by the device to acquire spatial polarization information. With the scheme of stacking ultrathin units along the optical path, it is expected to build multifunctional integrated devices without sacrificing the lateral single-pixel size, thus paving the way for next-generation ultracompact optical systems with diversified optical and optoelectronic applications.

## RESULTS

### Device design

The designed fiber-integrated polarimeter consists of three sequentially stacked functional units on a flat optical fiber endface, as schematically shown in Fig. 1A. Each unit includes a pair of asymmetrical electrodes against the fiber core for a self-driven effect, a layer of light-harvesting

[1]National Laboratory of Solid State Microstructures, College of Engineering and Applied Sciences, Collaborative Innovation Center of Advanced Microstructures, and Jiangsu Key Laboratory of Artificial Functional Materials, Nanjing University, Nanjing 210023, China. [2]Institute of Electromagnetics and Acoustics, Xiamen University, Xiamen 361005, China. [3]Research Center for Functional Materials, National Institute for Materials Science, 1-1 Namiki, Tsukuba 305-0044, Japan. [4]International Center for Materials Nanoarchitectonics, National Institute for Materials Science, 1-1 Namiki, Tsukuba 305-0044, Japan. [5]Hefei National Laboratory for Physical Sciences at Microscale and Department of Physics and CAS Key Laboratory of Strongly-coupled Quantum Matter Physics, University of Science and Technology of China, Hefei, Anhui 230026, China. [6]CAS Center for Excellence in Quantum Information and Quantum Physics, Hefei, Anhui 230026, China. [7]School of Physics and National Laboratory of Solid State Microstructures, Nanjing University, Nanjing 210093, China.
*Corresponding author. Email: haoyufeng@nju.edu.cn (Y.H.); feixu@nju.edu.cn (F.X.)
†These authors contributed equally to this work.

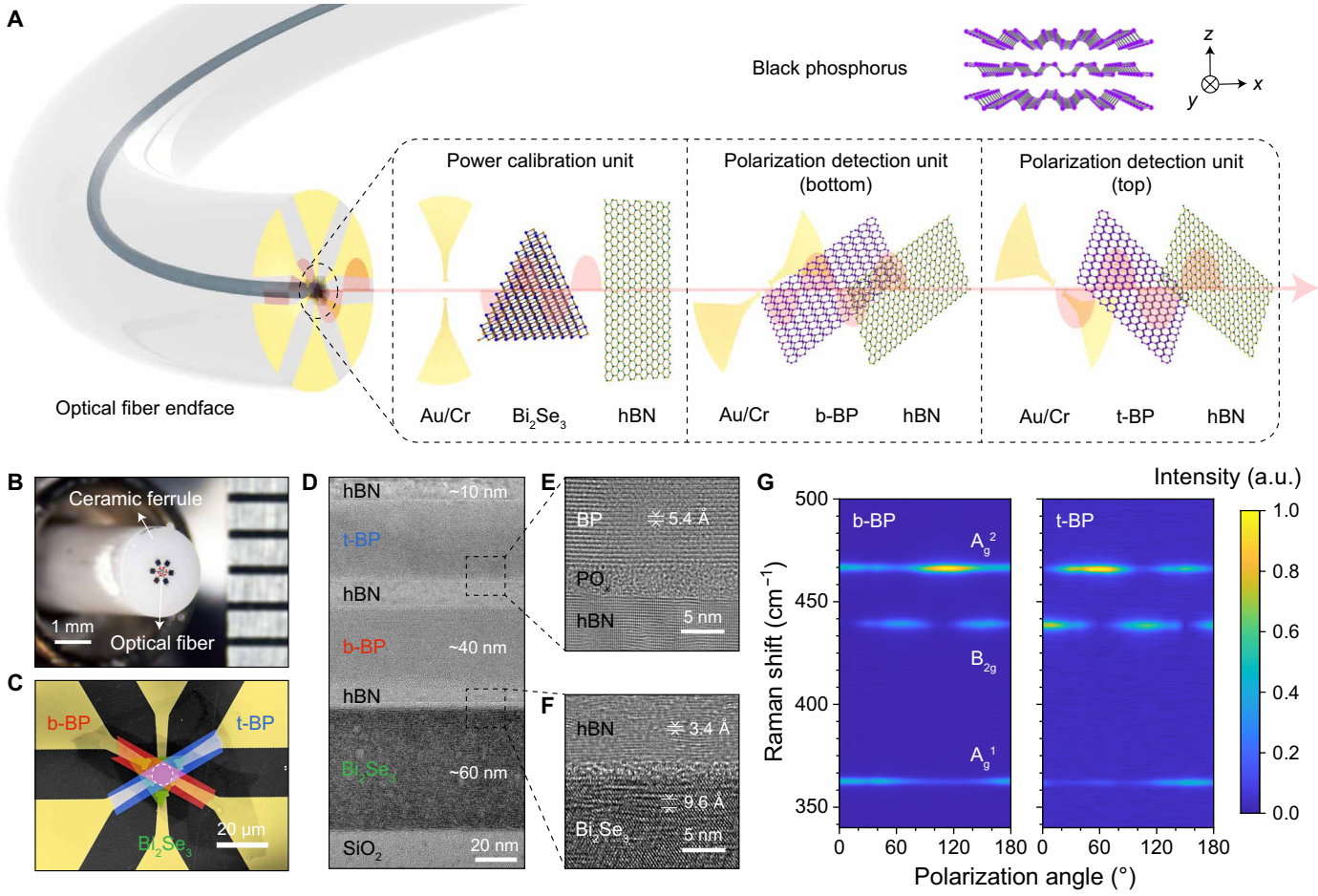


**Fig. 1. Structure of the fiber-integrated polarimeter.** (**A**) Schematic illustration of the designed fiber-integrated polarimeter. Three functional units are stacked subsequently onto an optical fiber endface. The top-right corner is the puckered honeycomb lattice of BP, where *x* and *y* present its armchair and zigzag crystal orientations, respectively, and *z* presents the stack direction of its layers. (**B**) Camera image of the polarimeter. The optical fiber is fixed in a ceramic ferrule with an outer diameter of 2.5 mm. (**C**) Pseudo-color scanning electron microscopy image of the stacked structures on the optical fiber endface. The white dashed circle represents the fiber core area. (**D**) Cross-sectional TEM image of the polarimeter. (**E** and **F**) High-resolution cross-sectional TEM images showing the BP/hBN and $Bi_2Se_3$/hBN interfaces, respectively. (**G**) Polarized Raman intensity mapping of the two twisted BP nanoflakes as a function of Raman shift and polarization angle. a.u., arbitrary units.

materials for functional photodetection, and a layer of hexagonal boron nitride (hBN) flakes for insulation and encapsulation. Since the photocurrent of an anisotropic material is influenced by both illumination power and polarization state, we use a polarization-insensitive isotropic $Bi_2Se_3$ layer at the bottom to calibrate incident light power and two twistedly stacked anisotropic BP layers for precise polarization sensing, substituting traditional mechanical rotation of polarizers. As shown in Fig. 1C, the intersection angles between the three pairs of electrodes are designed to be 60° (details in the Supplementary Materials), and the armchair crystal orientation of the BP is along the corresponding electrodes, presenting the high-mobility directions (*28*), which can be validated by Raman spectroscopy (Fig. 1G and fig. S2). A cross-sectional transmission electron micrograph (TEM) of a completed polarimeter is shown in Fig. 1D. The overall thickness of the vdW heterostructure is ~170 nm, consisting of a layer of ~60-nm-thick $Bi_2Se_3$, two layers of ~40-nm-thick BP, and three layers of ~10-nm-thick hBN. The high-resolution TEM images of the BP/hBN and $Bi_2Se_3$/hBN interfaces are shown in Fig. 1 (E and F, respectively). We can find that $Bi_2Se_3$ has a layered structure comprising a quintuple-layered unit cell with a thickness of 9.6 Å. The layered structure of BP and hBN can be seen clearly with an interlayer spacing of 5.4 and 3.3 Å, respectively. In addition, a thin amorphous layer of surface oxidation ($PO_x$) layer can also be observed at the BP/hBN interfaces, similar to previously reported BP samples, and even the major fabrication processes were carried out in an air-free environment (*8*).

## Photosensing performance

Before investigating the polarization analysis performance of the polarimeters, we test the primary photodetection performance of the component units. The relationship between illumination power *P* and polarization-insensitive photocurrent ($I_p = I_{light} - I_{dark}$) of $Bi_2Se_3$ can be well fitted as $I_p = mP^n$ (*m* and *n* are fitted constants), which is used to determine the power of incident light (fig. S8). As for the BP unit, when the initial polarization state (0°) of the incident light is fixed along the armchair direction of the BP, corresponding to the maximum polarized response (*8*), an obvious photocurrent can be observed at zero bias in the inset of Fig. 2A, revealing that the unit can work under bias-free conditions. Photoresponsivity (*R*)

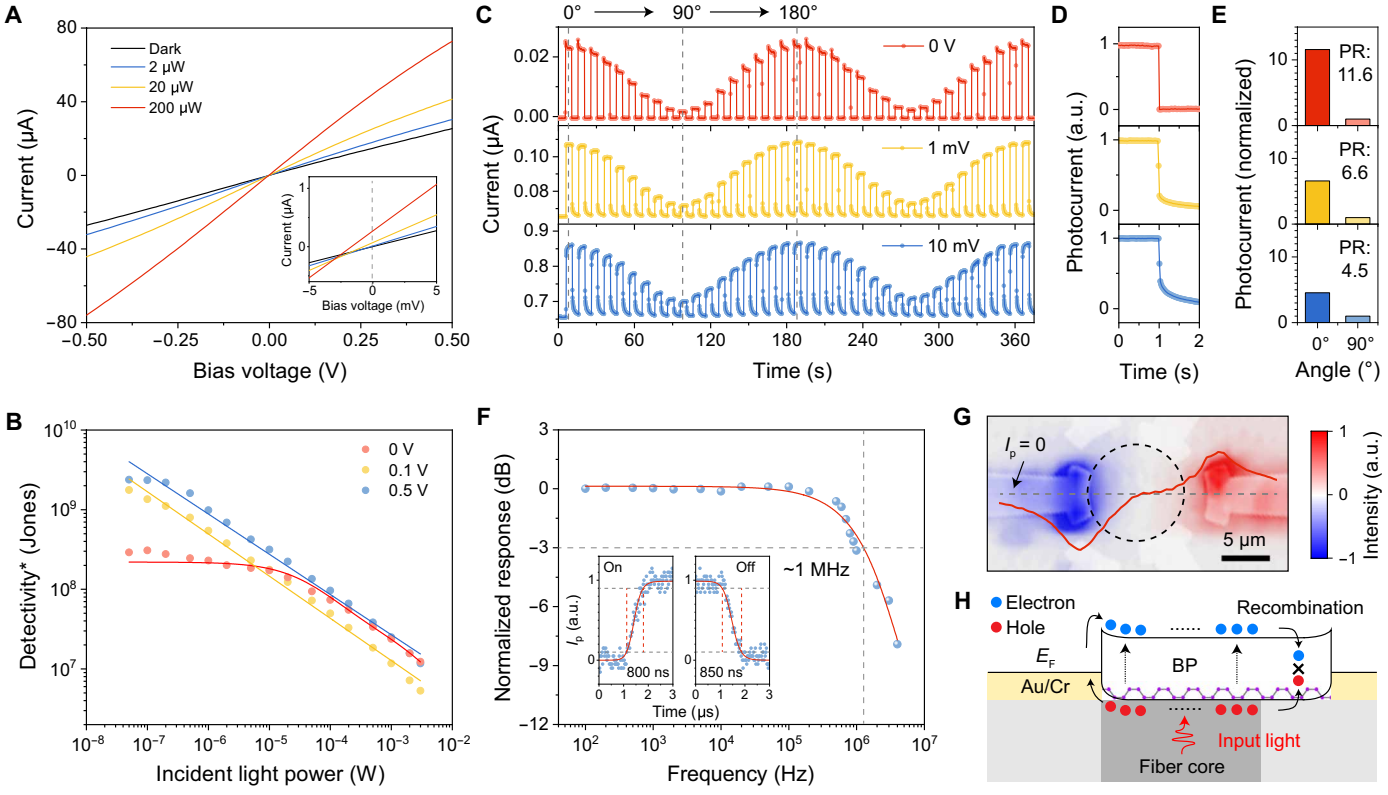


**Fig. 2. Photosensing performance of the BP unit (λ = 1550 nm).** (**A**) Current-voltage relation (*I-V*) curves as a function of illumination power. Inset: The enlarged view of the curves around zero bias. (**B**) Photodetectivity versus illuminating power under different bias voltages. The lines are fitting curves of measured data. (**C**) Bias voltage–dependent photoswitching performance under alternating dark and light illumination. The polarization angle of the incident light rotates by 10° after each light on-off cycle is completed. (**D**) Half cycles of photocurrent dynamics [from (C)] under different bias voltages. (**E**) Photocurrent generation versus bias voltages, which are varied for input light polarization along the *x* (0°) and *y* (90°) crystal orientations of BP. The photocurrents are normalized according to the photocurrent value under 90° polarized light. (**F**) Frequency response of the BP unit under zero bias, showing a −3-dB frequency of ~1 MHz. Inset: One cycle of photocurrent dynamics under zero bias. (**G**) Photocurrent mapping of the unit under zero bias. The black dashed circle represents the fiber core area. The red curve is the cross-sectional photocurrent profile along the gray dashed line. (**H**) Schematic of band diagram and photoexcited carrier transport under light illumination. The self-driven photosensing is based on the asymmetrical electrodes.

and photodetectivity ($D^*$) are key parameters to quantify the performance of a photodetector. Considering the huge difference in the dark current with and without bias, it is convincing to use $D^*$ to evaluate the photosensing performance of the BP units. The $D^*$ under different bias voltages in Fig. 2B shows near-linear curves at log-log coordinates, indicating the dominance of photogating effect caused by defects (*29*), while under zero bias, the photoresponsivity hardly decreases under a low illumination power because the defects in the BP crystal are not fully filled by photoinduced carriers. Here, regarding the bias-free condition, the unit shows a large $D^*$ of $2.91 \times 10^8$ Jones, owing to the strong suppression of the dark current.

Polarization ratio [PR; defined as the ratio of maximum and minimum polarized photoresponse (*21*)] and response time (τ) are also crucial figures of merit to evaluate the performance of a polarization-sensitive photodetector. Figure 2C shows the photoswitching performance of the BP unit with varied polarizations under three different bias voltages. We can find that, although a larger photocurrent is obtained with an external bias voltage, the response speed is much slower owing to the large drift current (Fig. 2D). Moreover, the PR of the BP unit under zero bias is larger than that under bias (Fig. 2E), beneficial for high-contrast polarization distinction.

Figure 2F shows the measured frequency response of ~1 MHz for the self-driven polarimeter. The rise and fall τ of the unit, measured under a 100-kHz modulation of light, are 800 and 850 ns, respectively. The response speed of the unit is fast among the reported BP-related photodetectors (*8*, *30*–*32*), which may stem from the specially designed asymmetric electrodes with efficient electron-hole separation near the BP-metal interface and the fast carrier recombination within the BP crystal away from the electrode (Fig. 2, G and H, discussed below). It is expected to further improve the response speed by avoiding the formation of a defective $PO_x$ layer at the BP-metal interface (*8*). In a brief summary, the self-driven mode of the BP unit shows a large $D^*$, a fast τ, a large PR, and a high on/off ratio (up to $10^3$).

To further illustrate the self-driven effect, Fig. 2G shows that the asymmetrical design of electrodes against the fiber core will result in a nonuniform illumination to the BP unit and generate spontaneous photocurrents. The corresponding energy diagrams in Fig. 2H explain that a Schottky junction is formed at the BP-metal interface and leads to a built-in electric field with a 160-meV potential difference (measured by the Kelvin probe force microscopy in fig. S3). The photoinduced electron-hole pairs generated at the illumination

area will diffuse to the region with a low carrier concentration. Due to the difference in the diffusion distance to the two electrodes, the recombination of carriers during the diffusion process results in the asymmetry of the number of carriers injected into the two electrodes, thus bringing a net photocurrent.

### Self-driven polarization analysis

Because of the overlap of the polarized photocurrent value within a period of polarization angles (0° to 180°), a single BP unit cannot fully distinguish all polarization states. Therefore, we investigate the polarimeter where two twisted BP units work together. We first demonstrate the LP light discernment of the polarimeter (Fig. 3A). The measured currents of the b-BP and t-BP can be well fitted with $I_b = a_1 + b_1\cos(2\theta)$ and $I_t = a_2 + b_2\cos(2\theta - 2\pi/3)$, respectively, where $a_1$, $b_1$ and $a_2$, $b_2$ are related to the light power and can be calculated with the assistance of the $Bi_2Se_3$ calibration unit. As expected, the polarized photocurrent curves of t-BP and b-BP show a 60° offset, in accordance with the polarized Raman results in Fig. 1D, indicating that the twisted crystal orientations of b-BP and t-BP are the reason for the difference in the polarized photocurrents. In addition, because of the weak light-matter interaction, the slight polarization conversion of the light transmitted from b-BP (due to the optical dichroism) shows little impact on the polarization photodetection of t-BP (*33*).

Besides the detection of LP light, the polarimeter enables the CP photoresponses. Because of the broken inversion symmetry of a material, the illumination of CP light onto the material results in a helicity-dependent photocurrent, which is called CPGE (*34*–*41*). In our polarimeter, the presence of anisotropic electric fields near the metal-BP contacts (originating from the Schottky barriers) will reduce the symmetry of the unit and result in a net CP photocurrent (*42*–*44*). In Fig. 3B, the helicity of incident light was continuously modulated by a quarter–wave plate (QWP), and the initial state of the QWP (0°) was set when the fast axis of the QWP coincided with the polarization direction of incident LP light. In a 180° QWP modulation period, the light goes through linear (0°)–left circular (45°)–linear (90°)–right circular (135°)–linear (180°) polarization states, and the photocurrent is found to change periodically with the change of light helicity. The generated photocurrent can be quantitatively expressed as

$$I = I_C \sin(2\varphi) + I_L \cos(4\varphi + \varphi_0) + I_0$$

where φ is the QWP angle, $I_C$ is the amplitude of the helicity-dependent CPGE current (green curves), $I_L$ is the amplitude of the linear polarization-sensitive LPGE current (yellow curves) with a phase shift $\varphi_0$ (affecting the shape of the photocurrent curves; fig. S10), and $I_0$ is the polarization-independent background current (*36*, *37*). It is obvious that CPGE currents (green curves) are generated in both

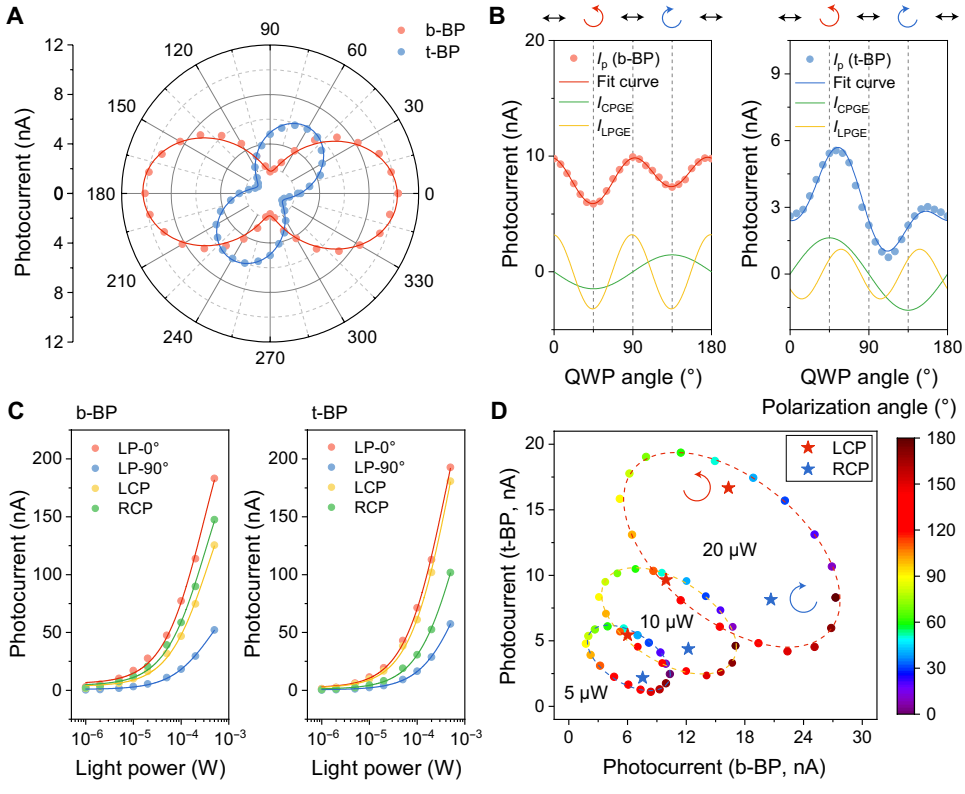


**Fig. 3. Unambiguous detection of LP and CP with the polarimeter.** (**A**) Polar plots of the polarized photocurrent generated in the two twisted BP units as a function of the linear polarization angle. The circles are experimental data, and the curves are fitted results. (**B**) One period of photocurrent of the twisted BP units as a function of QWP angle (red and blue curves). The extracted CPGE (green curves) and LPGE (yellow curves) are current components of the generated CP photocurrent. The red and blue circles are experimental data, and the curves are fitted results. (**C**) Photocurrents of the two BP units as functions of light power with different polarization states of incident light. (**D**) The 2D plot of photocurrent generated in the two twisted BP units under different polarization states. The results of LP light analysis fit well with the dashed ellipses. The three ellipses correspond to three different illumination powers.

BP units, whose direction can be reversed by changing the light polarization from left circular polarization (LCP; φ = 45°) to right circular polarization (RCP; φ = 135°).

Figure 3C shows the relationships between light power and generated photocurrent in the two BP units under different polarization states. By power calibration with the $Bi_2Se_3$ unit, we can obtain the maximum and minimum photocurrents in each BP unit during a period change of LP light states and thus establish sine equations. When the incident light is LP, the photocurrent data from b-BP ($I_b$) and t-BP ($I_t$) form a 2D parameter space that corresponds well to an elliptic equation

$$(aI_b + b)^2 + (cI_b + dI_t + e)^2 = 1$$

where $a$ to $e$ are constants related to the sine equations (details in the Supplementary Materials). Figure 3D shows the 2D plot of the measured photocurrent in the twisted BP units with the dots colored on the basis of the polarization state of light, which fully fill the calculated elliptic equations. As for the incident light being CP, the photocurrents generated by LCP or RCP states can be obtained by Fig. 3C, and the photocurrent data are shown as the intersection points, indicated with stars, of two straight lines in the $I_b$-$I_t$ parameter space. Therefore, the polarization state of an unknown LP or CP light can be unambiguously detected using the polarimeter with three cooperative units.

## Single-pixel polarimetric imaging

Single-pixel imaging is a computational imaging technique that needs only a single-pixel detector instead of a pixelated array detector (*45*, *46*). In this context, on the basis of the waveguide characteristics of optical fiber, our single-pixel polarimeter can be applied to achieve polarimetric imaging under different polarized illuminations by Hadamard single-pixel imaging (HSI) technique (more details in the Supplementary Materials) (*46*).

As shown in Fig. 4A, a polarized 1550-nm laser beam was modulated by a digital micromirror device (DMD) to generate a series of time-varying Hadamard encoded patterns. The Hadamard encoded patterns were sequentially projected onto the target object (CEAS), and the correlated light signals were detected by our polarimeter and converted to self-driven photocurrents. Our stacked device has two BP units twisted at 60°, which leads to a 60° offset of the LP response curves between two BP units (Fig. 3A). For HSI, the difference in response from t-BP and b-BP makes the single-pixel measurement values different, i.e., different self-driven photocurrents. Different self-driven photocurrents were used to reconstruct and normalize object images containing the polarization information of illuminations. As shown in Fig. 4 (B and C), because of the response characteristics of two BP units to LP light, the self-driven photocurrents and the intensity of reconstructed images under 45° and 135° polarizations are almost the same for the b-BP unit but show strong differences for the t-BP unit. Similar to the analysis of light polarization based on different photocurrents of twisted BPs, the different normalized intensities of reconstructed images of two BPs can also provide the polarization information of illumination light through the appropriate calibration. Therefore, by the cooperation of the twisted BP units, we can not only achieve object imaging but also distinguish the polarization of light by the appropriate calibration.

We further demonstrate the capability of the device for recognizing nonuniform polarization distribution of light field. As shown in Fig. 4D, the objects "CA" and "ES" were covered by two oriented

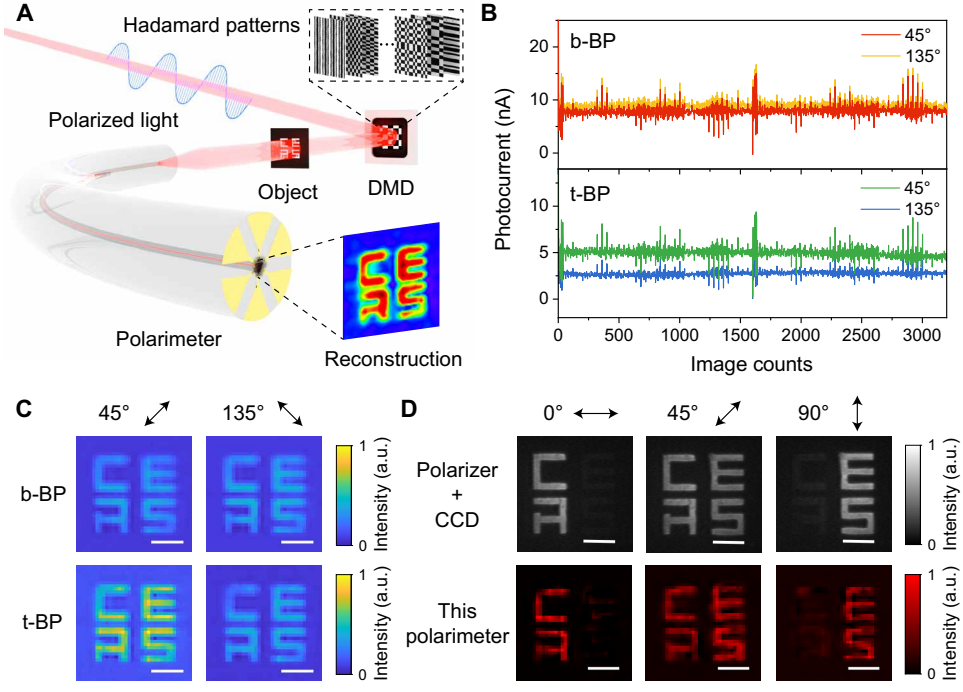


**Fig. 4. Single-pixel polarimetric imaging by the polarimeter.** (**A**) Schematic view of the experimental setup. (**B**) Self-driven photocurrents generated in both the bottom and top BP units under 45° and 135° LP illuminations. The initial polarization direction (0°) is fixed along with the armchair of b-BP. (**C**) Reconstructed polarimetric images of b-BP (top row of figures) and t-BP (bottom row of figures) under 45° and 135° LP illuminations. The image intensity was normalized on the basis of the photocurrent value. (**D**) Comparison of the images recorded by the CCD with a polarizer and the images (normalized intensity) reconstructed by the device under different LP illuminations. Scale bars (C and D), 1 mm.

tape films with a 45° difference (fig. S15), which can act analogously to a half–wave plate and change the polarization state of the transmitted light (*47*). Under different LP light illuminations, the object and the images reconstructed by the polarimeter (bottom row of Fig. 4D) are consistent with the images recorded by an infrared charge-coupled device (CCD) with a polarizer (top row of Fig. 4D). We note that the traditional division-of-focal-plane polarimeter structure requires at least four pixels in a group to acquire four polarization-dependent intensity components (0°, 45°, 90°, and 135°) of the incident light, whereas for our polarimeter, a single pixel can achieve similar results, thus showing potential for high-resolution and high-speed polarimetric imaging.

## DISCUSSION

We design and fabricate an ultracompact polarimeter by vdW stacking three 2D material units on fiber endfaces and demonstrate the polarization analysis and polarimetric imaging. The polarization state of an unknown LP or CP light can be directly and unambiguously detected using the polarimeter by obtaining the photocurrents generated in three cooperative detection units. Moreover, our polarimeter shows the ability to directly extract polarization information at a fast rate, free from extra polarization modulation and analysis devices, showing potential in high-speed polarization-division-multiplexed imaging and miniaturized, low-cost, real-time polarized endoscopy. The device performance can be further improved by strict environment control in the device preparation, testing, and storage environment to avoid BP oxidation. Moreover, a variety of 2D materials can be potential candidates, such as isotropic materials (graphene, transition metal dichalcogenides, etc.) and anisotropic materials [SnS, GeSe, $ReSe_2$, $ReS_2$, Te, etc. (*48*)]. The selection of metals in contact with the semiconductors can also be further optimized for faster response speed or stronger photogalvanic effects.

Notably, by stacking functional units along the optical path, a single pixel can be functionalized while maintaining the lateral size, which is especially critical for acquiring high-resolution images while obtaining more information of light. Meanwhile, we propose a universal method to design and fabricate complex structures on optical fiber endfaces with good manufactory stability and repeatability, bringing possibilities to assemble diversified integrated functional units, such as power meters (*49*), spectrometers (*50*), and modulators (*51*), onto the fiber endface to realize highly integrated multifunctional fiber-integrated systems.

## MATERIALS AND METHODS

### Materials preparation

We used a mechanical exfoliation method to prepare BP and hBN nanoflakes. In general, it is difficult to directly locate the *x*- and *y*-axis directions of mechanically exfoliated BP nanoflakes under a microscope. Thus, we used an oriented mechanical exfoliation method (fig. S1) where a BP bulk crystal with a clear crystal orientation underwent repeated mechanical exfoliation while maintaining the same crystal orientation. The oriented BP flakes were lastly transferred to polydimethylsiloxane (PDMS) for the next transfer step on the optical fiber endface.

The thickness of BP nanoflakes was evaluated by a TEM (FEI, Talos F200X) for ~40 nm. The thicker BP nanoflakes had a narrower bandgap, which was beneficial for infrared light-harvesting and demonstrated stronger light absorption. However, the BP nanoflakes cannot be too thick, which would lead to a large dark current, poor performance, low optical transmittance, and difficulties during the fabrication processes. To ensure insulation between the $Bi_2Se_3$, b-BP, and t-BP and avoid air exposure, few-layer hBN with a thickness of ~10 nm was used to separate and encapsulate these flakes.

We used a chemical vapor deposition system to synthesize $Bi_2Se_3$ nanoplates on mica substrates. Se powders (0.20 g) (99.9%, Alfa) in a ceramic boat were placed upstream of the quartz tube furnace (~220°C). A mica substrate was placed to cover the ceramic boat with $Bi_2Se_3$ powder (10 mg) in the center of the furnace. The quartz tube was purged with ultrahigh-purity argon (Ar) gas (99.999%) for 2 min, then ramped up to 560°C in 20 min, and held at 560°C for 10 min under a constant flow of Ar [30 standard cubic centimeters per minute (sccm)] and $H_2$ (10 sccm). After the reaction was completed, the furnace was cooled to room temperature, and the resulting materials grown on the mica substrate were collected for subsequent characterizations and processing.

The thickness of $Bi_2Se_3$ nanoplates was measured by a TEM for ~60 nm. The thicker $Bi_2Se_3$ nanoplates have higher mechanical strength, which were required in the transferring process. However, the $Bi_2Se_3$ nanoflakes cannot be too thick, which would lead to low optical transmittance and difficulties for the fabrication processes.

### EBL process on the fiber endface

To precisely fabricate the electrode structures on the optical fiber endface, we customized an optical fiber holder to allow the multistep spin coating processes on the fiber endface. In this process, three layers of resist films were coated, consisting of 9% methyl methacrylate (MMA) in ethyl lactate, 6% polymethyl methacrylate (PMMA) in anisole, and water-soluble polyaniline (AR-PC 5090) (fig. S5). Compared with PMMA, MMA was more sensitive to the electron beam. As a result, a trapezoidal exposure area was formed on the cross section of the resist after exposure. The electrodes on the optical fiber endface were then prepared by electron beam lithography (EBL; TESCAN, MIRA3), electron beam evaporation (VZZS-550, VNANO), and liftoff processes.

### Fabrication process of the device

As shown in fig. S6, after the preparation of electrodes on the fiber endface by EBL, Au/Cr deposition, and liftoff processes, $Bi_2Se_3$ and hBN on PDMS were transferred onto the electrodes by dry transfer method. Then, the b-BP and t-BP units were fabricated with a similar process.

### Measurement configurations

The experimental setup is demonstrated in fig. S7. An amplified spontaneous emission light source was used to provide an infrared laser with a 1530- to 1560-nm wavelength. The laser was coupled to an optical fiber, and a 90:10 optical fiber coupler was used to connect a power meter (S145C, Thorlabs) to monitor the light power. The laser wavelength was fixed at 1550 nm using a filter (FB1550-12, Thorlabs), and the polarization angle of incident light was fixed by a polarizer (FBR-LPNIR, Thorlabs) and changed by rotating a half–wave plate (FBR-AH3, Thorlabs) and a QWP (RABQ-1600, Thorlabs), which were both placed in a fiber bench (FB-76W, Thorlabs) with fiber ports (PAF-X-2-C, Thorlabs). The electrode pairs on the optical fiber endface were connected to digital source measure units (Keithley SMU 2450, Tektronix), whose negative electrodes were both grounded.

In the frequency response measurement, a signal generator (33522A, Agilent) and an electro-optic modulator (LN81S-FC, Thorlabs) were used to modulate the light, an amplifier (DLPCA-200, Femto) was used to magnify the photovoltage generated by the BP in self-driven mode, and an oscilloscope (MSOX6004A, Keysight) was used to monitor the high-frequency signal. Photocurrent mapping measurements were performed by a microscope system (alpha-300R, WITec). The polarimeter sample was fixed in the integrated microscope system, and the incident light was focused on the surface of the sample through the objective lens of the microscope and scanned in the *x*-*y* direction. The magnitudes of the device photocurrents corresponding to each *x*-*y* coordinate were recorded.

### Single-pixel polarimetric imaging

We used a 1550-nm laser (VFLS-1550, Connet) and DMD (DLP Discovery 3000, Vialux) to generate Hadamard basis patterns. The light was modulated by a polarizer (GCL-0510, Daheng Optics) and a half–wave plate (GCL-0604, Daheng Optics). Then, the light illuminated the target object and was collected by a fiber coupling system, and the photocurrent signals generated by the twisted BPs were collected and recorded by a source meter (Keithley SMU 2450, Tektronix). For single-pixel polarimetric imaging, Hadamard basis patterns were projected onto the target object, and the polarimetric images were reconstructed by differential HSI technique.

## SUPPLEMENTARY MATERIALS

Supplementary material for this article is available at https://science.org/doi/10.1126/sciadv.abo0375

## REFERENCES AND NOTES


1. N. A. Rubin, G. D'Aversa, P. Chevalier, Z. Shi, W. T. Chen, F. Capasso, Matrix Fourier optics enables a compact full-Stokes polarization camera. *Science* **365**, eaax1839 (2019).
2. O. Graydon, Global position by polarization. *Nat. Photonics* **12**, 318–318 (2018).
3. Z. Zhan, M. Cantono, V. Kamalov, A. Mecozzi, R. Müller, S. Yin, J. C. Castellanos, Optical polarization–based seismic and water wave sensing on transoceanic cables. *Science* **371**, 931–936 (2021).
4. A. Pors, M. G. Nielsen, S. I. Bozhevolnyi, Plasmonic metagratings for simultaneous determination of Stokes parameters. *Optica* **2**, 716–723 (2015).
5. C. Wang, G. Zhang, S. Huang, Y. Xie, H. Yan, The optical properties and plasmonics of anisotropic 2D materials. *Adv. Opt. Mater.* **8**, 1900996 (2019).
6. L. Li, W. Han, L. Pi, P. Niu, J. Han, C. Wang, B. Su, H. Li, J. Xiong, Y. Bando, T. Zhai, Emerging in-plane anisotropic two-dimensional materials. *InfoMat.* **1**, 54–73 (2019).
7. L. Li, P. Gong, D. Sheng, S. Wang, W. Wang, X. Zhu, X. Shi, F. Wang, W. Han, S. Yang, K. Liu, H. Li, T. Zhai, Highly in-plane anisotropic 2D $GeAs_2$ for polarization-sensitive photodetection. *Adv. Mater.* **30**, e1804541 (2018).
8. J. Bullock, M. Amani, J. Cho, Y.-Z. Chen, G. H. Ahn, V. Adinolfi, V. R. Shrestha, Y. Gao, K. B. Crozier, Y.-L. Chueh, A. Javey, Polarization-resolved black phosphorus/molybdenum disulfide mid-wave infrared photodiodes with high detectivity at room temperature. *Nat. Photonics* **12**, 601–607 (2018).
9. L. Ye, P. Wang, W. Luo, F. Gong, L. Liao, T. Liu, L. Tong, J. Zang, J. Xu, W. Hu, Highly polarization sensitive infrared photodetector based on black phosphorus-on-$WSe_2$ photogate vertical heterostructure. *Nano Energy* **37**, 53–60 (2017).
10. H. Yuan, X. Liu, F. Afshinmanesh, W. Li, G. Xu, J. Sun, B. Lian, A. G. Curto, G. Ye, Y. Hikita, Z. Shen, S. C. Zhang, X. Chen, M. Brongersma, H. Y. Hwang, Y. Cui, Polarization-sensitive broadband photodetector using a black phosphorus vertical p-n junction. *Nat. Nanotechnol.* **10**, 707–713 (2015).
11. L. Tong, X. Huang, P. Wang, L. Ye, M. Peng, L. An, Q. Sun, Y. Zhang, G. Yang, Z. Li, F. Zhong, F. Wang, Y. Wang, M. Motlag, W. Wu, G. J. Cheng, W. Hu, Stable mid-infrared polarization imaging based on quasi-2D tellurium at room temperature. *Nat. Commun.* **11**, 2308 (2020).
12. M. Peng, R. Xie, Z. Wang, P. Wang, W. Hu, Blackbody-sensitive room-temperature infrared photodetectors based on low-dimensional tellurium grown by chemical vapor deposition. *Sci. Adv.* **7**, eabf7358 (2021).
13. C. Fang, J. Li, B. Zhou, D. Li, Self-powered filterless on-chip full-stokes polarimeter. *Nano Lett.* **21**, 6156–6162 (2021).
14. X. Wang, Y. Li, L. Huang, X. W. Jiang, L. Jiang, H. Dong, Z. Wei, J. Li, W. Hu, Short-wave near-infrared linear dichroism of two-dimensional germanium selenide. *J. Am. Chem. Soc.* **139**, 14976–14982 (2017).
15. Y. Liu, B. N. Shivananju, Y. Wang, Y. Zhang, W. Yu, S. Xiao, T. Sun, W. Ma, H. Mu, S. Lin, H. Zhang, Y. Lu, C. W. Qiu, S. Li, Q. Bao, Highly efficient and air-stable infrared photodetector based on 2D layered graphene-black phosphorus heterostructure. *ACS Appl. Mater. Interfaces* **9**, 36137–36145 (2017).
16. F. Xia, H. Wang, J. C. M. Hwang, A. H. C. Neto, L. Yang, Black phosphorus and its isoelectronic materials. *Nat. Rev. Phys.* **1**, 306–317 (2019).
17. X. Chen, X. Lu, B. Deng, O. Sinai, Y. Shao, C. Li, S. Yuan, V. Tran, K. Watanabe, T. Taniguchi, D. Naveh, L. Yang, F. Xia, Widely tunable black phosphorus mid-infrared photodetector. *Nat. Commun.* **8**, 1672 (2017).
18. T. Akamatsu, T. Ideue, L. Zhou, Y. Dong, S. Kitamura, M. Yoshii, D. Yang, M. Onga, Y. Nakagawa, K. Watanabe, T. Taniguchi, J. Laurienzo, J. Huang, Z. Ye, T. Morimoto, H. Yuan, Y. Iwasa, A van der Waals interface that creates in-plane polarization and a spontaneous photovoltaic effect. *Science* **372**, 68–72 (2021).
19. T. J. Echtermeyer, L. Britnell, P. K. Jasnos, A. Lombardo, R. V. Gorbachev, A. N. Grigorenko, A. K. Geim, A. C. Ferrari, K. S. Novoselov, Strong plasmonic enhancement of photovoltage in graphene. *Nat. Commun.* **2**, 458 (2011).
20. J. Wei, Y. Li, L. Wang, W. Liao, B. Dong, C. Xu, C. Zhu, K.-W. Ang, C.-W. Qiu, C. Lee, Zero-bias mid-infrared graphene photodetectors with bulk photoresponse and calibration-free polarization detection. *Nat. Commun.* **11**, 6404 (2020).
21. J. Wei, C. Xu, B. Dong, C.-W. Qiu, C. Lee, Mid-infrared semimetal polarization detectors with configurable polarity transition. *Nat. Photonics* **15**, 614–621 (2021).
22. M. Jung, S. Dutta-Gupta, N. Dabidian, I. Brener, M. Shcherbakov, G. Shvets, Polarimetry using graphene-integrated anisotropic metasurfaces. *ACS Photonics* **5**, 4283–4288 (2018).
23. L. Li, J. Wang, L. Kang, W. Liu, L. Yu, B. Zheng, M. L. Brongersma, D. H. Werner, S. Lan, Y. Shi, Y. Xu, X. Wang, Monolithic full-stokes near-infrared polarimetry with chiral plasmonic metasurface integrated graphene-silicon photodetector. *ACS Nano* **14**, 16634–16642 (2020).
24. F. Wang, L. Li, W. Huang, L. Li, B. Jin, H. Li, T. Zhai, Submillimeter 2D $Bi_2Se_3$ flakes toward high-performance infrared photodetection at optical communication wavelength. *Adv. Funct. Mater.* **28**, 1802707 (2018).
25. J. Qiao, X. Kong, Z. X. Hu, F. Yang, W. Ji, High-mobility transport anisotropy and linear dichroism in few-layer black phosphorus. *Nat. Commun.* **5**, 4475 (2014).
26. L. Li, Y. Yu, G. J. Ye, Q. Ge, X. Ou, H. Wu, D. Feng, X. H. Chen, Y. Zhang, Black phosphorus field-effect transistors. *Nat. Nanotechnol.* **9**, 372–377 (2014).
27. L. Li, J. Kim, C. Jin, G. J. Ye, D. Y. Qiu, F. H. da Jornada, Z. Shi, L. Chen, Z. Zhang, F. Yang, K. Watanabe, T. Taniguchi, W. Ren, S. G. Louie, X. H. Chen, Y. Zhang, F. Wang, Direct observation of the layer-dependent electronic structure in phosphorene. *Nat. Nanotechnol.* **12**, 21–25 (2017).
28. F. Xia, H. Wang, Y. Jia, Rediscovering black phosphorus as an anisotropic layered material for optoelectronics and electronics. *Nat. Commun.* **5**, 4458 (2014).
29. M. Buscema, J. O. Island, D. J. Groenendijk, S. I. Blanter, G. A. Steele, H. van der Zant, A. Castellanos-Gomez, Photocurrent generation with two-dimensional van der Waals semiconductors. *Chem. Soc. Rev.* **44**, 3691–3718 (2015).
30. M. Huang, M. Wang, C. Chen, Z. Ma, X. Li, J. Han, Y. Wu, Broadband black-phosphorus photodetectors with high responsivity. *Adv. Mater.* **28**, 3481–3485 (2016).
31. Q. Guo, A. Pospischil, M. Bhuiyan, H. Jiang, H. Tian, D. Farmer, B. Deng, C. Li, S. J. Han, H. Wang, Q. Xia, T. P. Ma, T. Mueller, F. Xia, Black phosphorus mid-infrared photodetectors with high gain. *Nano Lett.* **16**, 4648–4655 (2016).
32. M. Buscema, D. J. Groenendijk, S. I. Blanter, G. A. Steele, H. van der Zant, A. Castellanos-Gomez, Fast and broadband photoresponse of few-layer black phosphorus field-effect transistors. *Nano Lett.* **14**, 3347–3352 (2014).
33. S. Biswas, M. Y. Grajower, K. Watanabe, T. Taniguchi, H. A. Atwater, Broadband electro-optic polarization conversion with atomically thin black phosphorus. *Science* **374**, 448–453 (2021).
34. Z. Ni, K. Wang, Y. Zhang, O. Pozo, B. Xu, X. Han, K. Manna, J. Paglione, C. Felser, A. G. Grushin, F. de Juan, E. J. Mele, L. Wu, Giant topological longitudinal circular photo-galvanic effect in the chiral multifold semimetal CoSi. *Nat. Commun.* **12**, 154 (2021).
35. L. Luo, D. Cheng, B. Song, L. L. Wang, C. Vaswani, P. M. Lozano, G. Gu, C. Huang, R. H. J. Kim, Z. Liu, J. M. Park, Y. Yao, K. Ho, I. E. Perakis, Q. Li, J. Wang, A light-induced phononic symmetry switch and giant dissipationless topological photocurrent in $ZrTe_5$. *Nat. Mater.* **20**, 329–334 (2021).
36. Z. Ji, G. Liu, Z. Addison, W. Liu, P. Yu, H. Gao, Z. Liu, A. M. Rappe, C. L. Kane, E. J. Mele, R. Agarwal, Spatially dispersive circular photogalvanic effect in a Weyl semimetal. *Nat. Mater.* **18**, 955–962 (2019).
37. H. Yuan, X. Wang, B. Lian, H. Zhang, X. Fang, B. Shen, G. Xu, Y. Xu, S. C. Zhang, H. Y. Hwang, Y. Cui, Generation and electric control of spin-valley-coupled circular photogalvanic current in WSe2. *Nat. Nanotechnol.* **9**, 851–857 (2014).

38. S. Zhang, N. Tang, W. Jin, J. Duan, X. He, X. Rong, C. He, L. Zhang, X. Qin, L. Dai, Y. Chen, W. Ge, B. Shen, Generation of Rashba spin-orbit coupling in CdSe nanowire by ionic liquid gate. *Nano Lett.* **15**, 1152–1157 (2015).
39. Y. Xie, L. Zhang, Y. Zhu, L. Liu, H. Guo, Photogalvanic effect in monolayer black phosphorus. *Nanotechnology* **26**, 455202 (2015).
40. Z. Ji, W. Liu, S. Krylyuk, X. Fan, Z. Zhang, A. Pan, L. Feng, A. Davydov, R. Agarwal, Photocurrent detection of the orbital angular momentum of light. *Science* **368**, 763–767 (2020).
41. M. M. Ramin Moayed, F. Li, P. Beck, J. C. Schober, C. Klinke, Anisotropic circular photogalvanic effect in colloidal tin sulfide nanosheets. *Nanoscale* **12**, 6256–6262 (2020).
42. J. Quereda, J. Hidding, T. S. Ghiasi, B. J. van Wees, C. H. van der Wal, M. H. D. Guimarães, The role of device asymmetries and Schottky barriers on the helicity-dependent photoresponse of 2D phototransistors. *npj 2D Mater. Appl.* **5**, 13 (2021).
43. M. M. Ramin Moayed, T. Bielewicz, M. S. Zollner, C. Herrmann, C. Klinke, Towards colloidal spintronics through Rashba spin-orbit interaction in lead sulphide nanosheets. *Nat. Commun.* **8**, 15721 (2017).
44. S. Dhara, E. J. Mele, R. Agarwal, Voltage-tunable circular photogalvanic effect in silicon nanowires. *Science* **349**, 726–729 (2015).
45. M. P. Edgar, G. M. Gibson, M. J. Padgett, Principles and prospects for single-pixel imaging. *Nat. Photonics* **13**, 13–20 (2018).
46. Z. Zhang, X. Wang, G. Zheng, J. Zhong, Hadamard single-pixel imaging versus Fourier single-pixel imaging. *Opt. Express* **25**, 19619–19639 (2017).
47. V. Durán, P. Clemente, M. Fernández-Alonso, E. Tajahuerce, J. Lancis, Single-pixel polarimetric imaging. *Opt. Lett.* **37**, 824–826 (2012).
48. G. P. Neupane, K. Zhou, S. Chen, T. Yildirim, P. Zhang, Y. Lu, In-plane isotropic/anisotropic 2D van der Waals heterostructures for future devices. *Small* **15**, e1804733 (2019).
49. J. H. Chen, Z. H. Liang, L. R. Yuan, C. Li, M. R. Chen, Y. D. Xia, X. J. Zhang, F. Xu, Y. Q. Lu, Towards an all-in fiber photodetector by directly bonding few-layer molybdenum disulfide to a fiber facet. *Nanoscale* **9**, 3424–3428 (2017).
50. S. Yuan, D. Naveh, K. Watanabe, T. Taniguchi, F. Xia, A wavelength-scale black phosphorus spectrometer. *Nat. Photonics* **15**, 601–607 (2021).
51. K. Y. Lau, A. Pyymaki Perros, D. Li, M. Kim, Z. Sun, Scalable graphene electro-optical modulators for all-fibre pulsed lasers. *Nanoscale* **13**, 9873–9880 (2021).
52. F. Qin, F. Gao, M. Dai, Y. Hu, M. Yu, L. Wang, W. Feng, B. Li, P. Hu, Multilayer InSe-Te van der Waals heterostructures with an ultrahigh rectification ratio and ultrasensitive photoresponse. *ACS Appl. Mater. Interfaces* **12**, 37313–37319 (2020).
53. G. Wang, L. Li, W. Fan, R. Wang, S. Zhou, J.-T. Lü, L. Gan, T. Zhai, Photodetectors: Interlayer coupling induced infrared response in $WS_2/MoS_2$ heterostructures enhanced by surface plasmon resonance. *Adv. Funct. Mater.* **28**, 1800339 (2018).
54. A. Castellanos-Gomez, M. Buscema, R. Molenaar, V. Singh, L. Janssen, H. S. J. van der Zant, G. A. Steele, Deterministic transfer of two-dimensional materials by all-dry viscoelastic stamping. *2D Mater.* **1**, 011002 (2014).
55. M. A. Meitl, Z.-T. Zhu, V. Kumar, K. J. Lee, X. Feng, Y. Y. Huang, I. Adesida, R. G. Nuzzo, J. A. Rogers, Transfer printing by kinetic control of adhesion to an elastomeric stamp. *Nat. Mater.* **5**, 33–38 (2005).
56. K. Kim, M. Yankowitz, B. Fallahazad, S. Kang, H. C. P. Movva, S. Huang, S. Larentis, C. M. Corbet, T. Taniguchi, K. Watanabe, S. K. Banerjee, B. J. Le Roy, E. Tutuc, Van der Waals heterostructures with high accuracy rotational alignment. *Nano Lett.* **16**, 1989–1995 (2016).
57. X. Gong, M. Tong, Y. Xia, W. Cai, J. S. Moon, Y. Cao, G. Yu, C. L. Shieh, B. Nilsson, A. J. Heeger, High-detectivity polymer photodetectors with spectral response from 300 nm to 1450 nm. *Science* **325**, 1665–1667 (2009).
58. D. Li, H. Jussila, L. Karvonen, G. Ye, H. Lipsanen, X. Chen, Z. Sun, Polarization and thickness dependent absorption properties of black phosphorus: New saturable absorber for ultrafast pulse generation. *Sci. Rep.* **5**, 15899 (2015).


**Acknowledgments:** We thank P. Chen and W. Hu for help in the work. **Funding:** This research was sponsored by the National Key R&D Program of China (2021YFA1401103 and 2018YFA0305800), the National Natural Science Foundation of China (61925502, 51772145, and 62135007), the Natural Science Foundation of Jiangsu Province (grant no. BK20180003), and the 333 high level talent training project of Jiangsu province. K.W. and T.T. acknowledge support from the Elemental Strategy Initiative conducted by the MEXT, Japan (grant no. JPMXP0112101001) and JSPS KAKENHI (grant nos. JP19H05790 and JP20H00354). **Author contributions:** F.X. and Y.H. conceived the idea, designed the experiments, and guided the research. Y.X., Y.W., H.X., C.W., and Y.M. fabricated and measured the devices. R.Z., Y.X., Y. Liu, and Y.C. performed the single-pixel imaging experiments. Y.W. and Y.X. characterized the materials. Y.X., Y.W., and R.Z. analyzed the data. X.C. and M.S. grew the BP crystals. T.T. and K.W. grew the hBN crystals. Y.H., F.X., and P.Z. advised on the experiments. Y.X., Y.W., and R.Z. wrote the original draft. F.X., Y.H., P.Z., J.C., and Y. Lu edited the manuscript. Y.X., Y.W., R.Z., F.X., Y.H., and Y. Lu prepared the response. All the authors reviewed and advised on both the original and revised manuscripts. **Competing interests:** The authors declare that they have no competing interests. **Data and materials availability:** All data needed to evaluate the conclusions in the paper are present in the paper and/or the Supplementary Materials.

Submitted 10 January 2022
Accepted 17 March 2022
Published 4 May 2022
10.1126/sciadv.abo0375